Low-temperature quantum magnetotransport of graphene on SiC (0 0 0 1) in pulsed magnetic fields up to 30 T

Lähderanta E., Lebedev A. A., Shakhov M. A., Stamov V. N., Lisunov K. G., Lebedev S. P.

DOI: 10.1088/1361-648X/ab5bb6

Low-temperature quantum magnetotransport of graphene on SiC (0001) in pulsed magnetic fields up to 30 T

E Lähderanta[1], A A Lebedev[2], M A Shakhov[1,2], V N Stamov[1], K G Lisunov[1,3] and S P Lebedev[2]

[1] Department of Physics, LUT University, PO Box 20, FIN-53851, Lappeenranta, Finland.

[2] Ioffe Institute, Politehnicheskaya Str. 26, St. Petersburg, 194021, Russian Federation.

[3] Institute of Applied Physics, Academiei Str. 5, MD-2028, Chisinau, Republic of Moldova.

E-mail: kgl-official@hotmail.com

Abstract

Resistivity, ρ (*T*), and magnetoresistance (MR) are investigated in graphene grown on SiC (0001), at temperatures between $T \sim 4 - 85$ K in pulsed magnetic fields of B up to 30 T. According to the Raman spectroscopy and Kelvin-probe microscopy data, the material is a single-layer graphene containing ~ 20 % double-layer islands with a submicron scale and relatively high amount of intrinsic defects. The dependence of ρ (*T*) exhibits a minimum at temperature $T_m \sim 30$ K. The low-field Hall data have yielded a high electron concentration, $n_R \approx 1.4\times10^{13}$ cm^{-2} connected to intrinsic defects, and a mobility value of $\mu_H \sim 300$ cm^2/(Vs) weakly depending on *T*. Analysis of the Shubnikov-de Haas oscillations of MR, observed between $B \sim 10 - 30$ T, permitted to establish existence of the Berry phase $\beta \approx 0.55$ and the cyclotron mass, $m_c \approx 0.07$ (in units of the free electron mass) close to expected values for the single-layer graphene, respectively. MR at 4.2 K is negative up to $B \sim 9$ T, exhibiting a minimum near 3 T. Analysis of MR within the whole range of $B = 0 - 10$ T below the onset of the SdH effect has revealed three contributions, connected to (i) the classical MR effect, (ii) the weak localization, and (iii) the electron-electron interaction. Analysis of the ρ (*T*) dependence has confirmed the presence of the contributions (ii) and (iii), revealing a high importance of the electron-electron scattering. As a result, characteristic relaxation times were obtained; an important role of the spin-orbit interaction in the material has been demonstrated, too.

Keywords: graphene, magnetotransport, negative magnetoresistance, Shubnikov-de Haas effect

1. Introduction

Graphene, representing a separate single-atomic graphite layer, acquired a great attention during the last decade. This material exhibits unique electronic properties, making graphene to be one of the most promising two-dimensional (2D) materials for nanoelectronic applications [1]. The perfect graphene is a massless and gapless Dirac quasiparticle system with a linear energy spectrum, differing strongly from other 2D electron systems [2].

Preparation of graphene can be performed mainly by the following processes: (i) graphite exfoliation [3], (ii) chemical vapor deposition on metal substrates [4], and (iii) thermal destruction of the SiC surface [5, 6]. Although graphene has been investigated extensively to the present time, its properties are studied preferably using single graphene layers, prepared by a mechanical deposition on a substrate. On the other hand, a lesser attention has been paid for the graphene grown on substrates, leading to insufficient understanding of its specifics. In turn, the properties of graphene in latter case may depend strongly on a choice of the substrate and on the character of binding to the substrate [7].

On the other hand, one of the most promising technology for synthesis of graphene is connected to a thermal destruction of the semi-insulating silicon carbide (SiC) substrate surface. On this way, one can obtain material with high quality and relatively large sizes, which give a better possibility for its industrial utilizations. Although such structures have been already studied [5, 6], the understanding of the role of interfacial layer in the graphene properties is still insufficient. The point is that the carrier mobility in these materials is much lower than in the mechanically deposited graphene layers, due to a high level of defects existing in the interface. Therefore, observations of the quantum effects in conductivity, such as the Shubnikov-de Haas (SdH) effect usually are much more problematic [8].

Here, we investigate the resistivity, ρ (T), and the magnetoresistance (MR) of graphene obtained with the thermal destruction method on the SiC (0001) surface in argon. The purpose is observation of a possible manifestations of quantum magnetotransport effects, including the SdH oscillations, the weak localization (WL) and the electron-electron interaction (EEI) leading to the negative (nMR) or anomalous positive (pMR) contributions to MR [2, 7]. For such a purpose, the low-temperature interval of $T \sim 4 - 85$ K, accompanied with pulsed magnetic fields up to 30 T has been chosen, and a detailed quantitative analysis of the ρ (T) and MR data has been performed.

2. Materials and methods

Graphene films were grown by using the method of thermal decomposition of the silicon carbide surface in an inert gas (argon). The following technological growth parameters were used: growth temperature of 1750 ± 20 ° C, growth time of 5 min, and argon pressure in the chamber of 760 ± 10 Torr. The substrates were high-resistive SiC of the 4H polytype, oriented along the Si face (0001). The characterization of the grown graphene material was performed with Raman spectroscopy, atomic-force microscopy (AFM), and Kelvin-probe microscopy methods [9]. Because of the high importance of the corresponding data, the main results are reproduced below (see Ref. 9 for details).

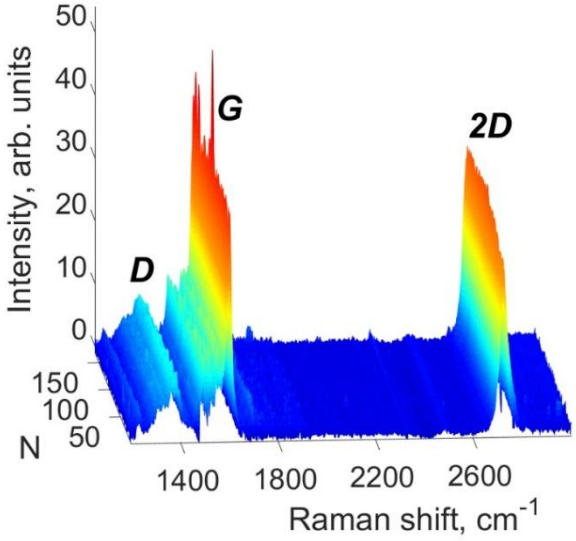

Figure 1. Raman spectra for graphene grown on the Si face of 4H-SiC. The substrate spectrum contribution is subtracted from the original array of spectra [9].

The array of Raman spectra with a total number of $N = 121$, measured on a sample area of 10×10 μm^2, is shown in figure 1 [9]. These spectra exhibits features emerging upon light scattering from the graphene film, including G and 2D lines and a weaker D line [3]. The latter, not existing in a perfect (pristine) graphene, has a disorder-induced nature and is connected to different kinds of symmetry-breaking defects, including point defects, graphene edges and impurities [2, 10]. Therefore, its presence in the spectrum of figure 1 indicates a relatively large amount of intrinsic defects in our material. The analysis of the G line intensity map, obtained by processing the array, has demonstrated

sufficiently uniform distribution of the line intensity over the sample area. This characterizes a good thickness uniformity of the graphene film in the analyzed region. The 2D line in the majority of spectra was found to be symmetric and can be fitted well with a single Lorentzian function, indicative of a single-layer graphene [11, 12]. On the other hand, in less than ~ 20 - 25 % of spectra is observed 2D line shape, which requires approximation with a pack of four Lorentzians functions. As follows from the analysis of the 2D line shape, the sample is formed mainly by a single-layer graphene containing ~ 20 % of double-layer inclusions.

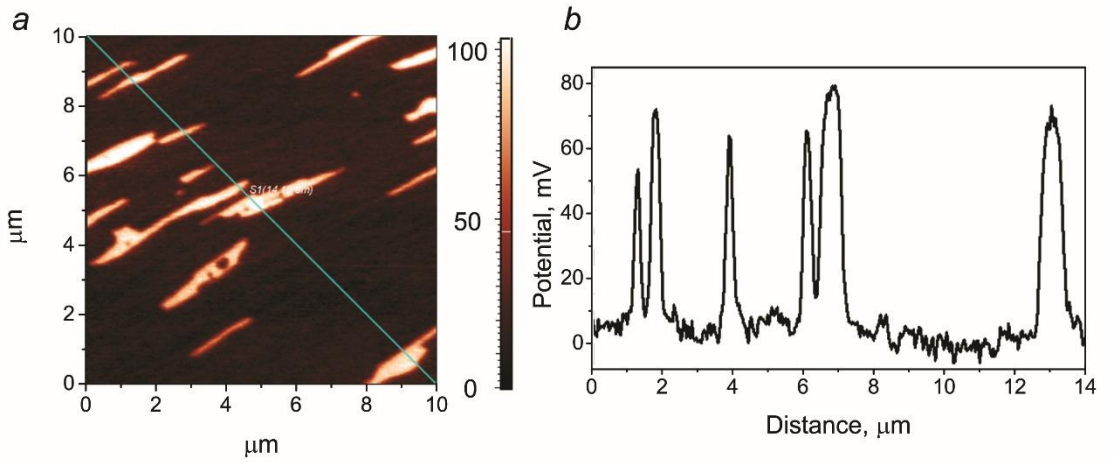

Figure 2. (a) The distribution of the surface potential for graphene grown on the Si face of 4H-SiC. (b) The profile of the surface potential, measured along the dashed line in Figure 2 (a) [9].

As can be seen in figure 2 (a) [9], the distribution of the surface potential obtained by the Kelvin-probe microscopy exhibits bright regions, connected to an increased surface potential, in a form of elongated strips. Their direction coincides with the direction of the terraces in the topographic image. The area of the bright regions is less than ~ 20 - 25% of the image area. The potential difference between the bright and dark regions in figure 2 (b) is found to be 80 mV, corresponding to the surface potential difference of the single-layer and the double-layer graphene [12]. In figure 2 (a), the bright regions are identified as the double-layer graphene. Such inference is in agreement with the data of the Raman investigations performed within the same sample area.

The Hall bar test structure was prepared on the surface of the graphene film with thickness of 1 nm for electrical measurements. Patterns for the Hall bars and the contacts were made using laser photolithography with AZ5214 resist. Reactive ion etching in argon–oxygen plasma was applied to remove the graphene layer from the uncoated areas. Device with the channel size of 2200μm × 300

μm was fabricated on a 1mm×5mm chip. Stable and low-resistance contacts were fabricated by a two-step Ti/Au (5/50 nm) metallization process using e-beam lithography and liftoff photolithography. More details of sample processing are described in Ref. 13.

For the MR measurements, a pulsed magnetic field (PMF) was applied, and the sample temperature was controlled using a filling helium cryostat. To avoid any induced voltage pertinent of the PMF measurements, a dual compensation method, including the hardware and the software component, was used. More details about the PMF measurement procedure and the installation parameters could be found elsewhere [14].

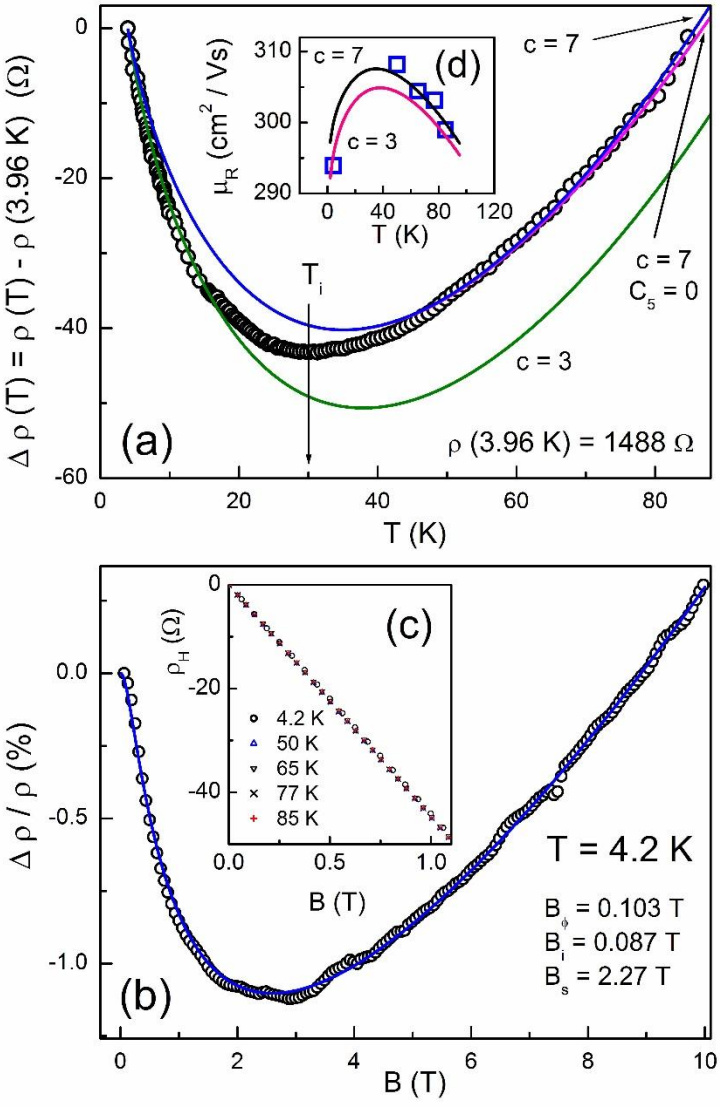

Figure 3. Temperature dependence of the resistivity in zero magnetic field (a). The dependence of $\Delta\rho/\rho$ on B at 4.2 K (b). The plots of ρ_H vs. B at different temperatures (c). The dependence of μ_R on T (d). The lines are calculated as described in the text.

3. Results and analysis

As can be seen in figure 3 (a), the resistivity ρ (*T*) in zero magnetic field exhibits a clear minimum at temperature $T_m \approx 30$ K. The reasons that we plot the difference of $\Delta\rho = \rho(T) - \rho(3.96\ \text{K})$ in figure 3 (a) will be clear later. In non-zero field, MR defined as $\Delta\rho/\rho \equiv [\rho(B) - \rho(0)] / \rho(0)$ is negative almost within the whole field interval of $B \sim 0 - 10$ T, where the magnetic quantization of the electron energy spectrum is unimportant, which is evident in figure 3 (b). In addition, MR attains a minimum at $B_{min} \sim 3$ T, and becomes positive with increasing *B* above ~ 9 T. With further increasing

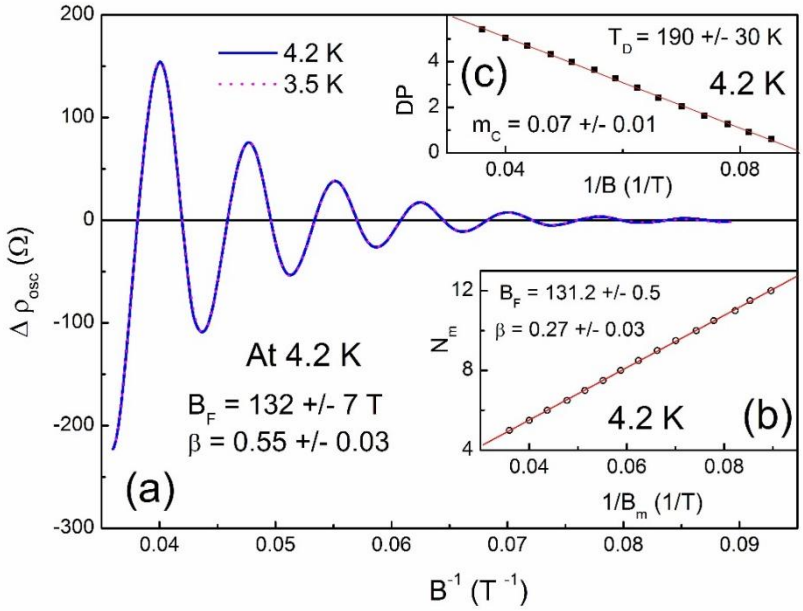

Figure 4. (a) The dependence of $\Delta\rho_{osc}$ on B^{-1}; (b) the fan plot of N_m vs. $1/B_m$; (c) The Dingle plot, DP vs. $1/B$. The lines in (b, c) are linear fits.

field, the SdH oscillations of MR set in, as shown in figure 4 (a). As can be seen in Fig. 3 (c), the low-field Hall resistivity, ρ_H, is a linear function of *B*. The Hall coefficient, R_H, is negative indicating *n*-type conductivity, and exhibiting a weak but rather irregular temperature increase inside the values of $R_H = (4.45 \pm 0.05)\times10^5$ cm^2/C, corresponding to the Hall concentration $n_R = (1.40 \pm 0.01)\times10^{13}$ cm^{-2}. The Hall mobility, μ_R, also demonstrates a weak dependence on *T* in the interval of $\mu_R = (302 \pm 5)$ cm^2 /(Vs), but in a more regular way, having a maximum near 50 K, as can be seen in figure 3 (d).

3.1. Analysis of the SdH effect

The oscillating part of the resistivity, $\Delta \rho_{osc}$, presented vs. reciprocal field in figure 4 (a), has been obtained after subtraction of the weak MR background. One can see practically no difference between the data observed at 3.5 and 4.2 K, revealing a quite weak dependence of the SdH oscillations on *T*. The latter is in line with the literature data of the SdH effect in graphene at low temperatures [5, 9, 15 − 18]. The fast Fourier transform (FFT) image of the data at 3.5 K is displayed in figure 5, including the FFT amplitude and phase shown in figures 5 (a) and 5 (b), respectively. A clear maximum, attributable to the first SdH harmonic amplitude, can be seen at the frequency B_F = 132 ± 7 T, corresponding to the phase $\varphi = 378 \pm 23^{\circ}$ or $\gamma = 1.05 \pm 0.06$ (in units of 2π) and $\beta \equiv \gamma - 1/2 = 0.55 \pm 0.03$. The value of β is quite close to the Berry phase, $\beta = 1/2$ expected in graphene [2]. The SdH concentration, $n_{SdH} = 2e B_F / (\pi \hbar)$, where *e* is the elementary charge and ħ is the Planck constant [2], is close to n_R but somewhat lower, $n_{SdH} = (1.27 \pm 0.07) \times 10^{13}$ cm^{-2}. The difference of the data above from those obtained at 4.2 K is negligible, as can be expected from figure 4 (a).

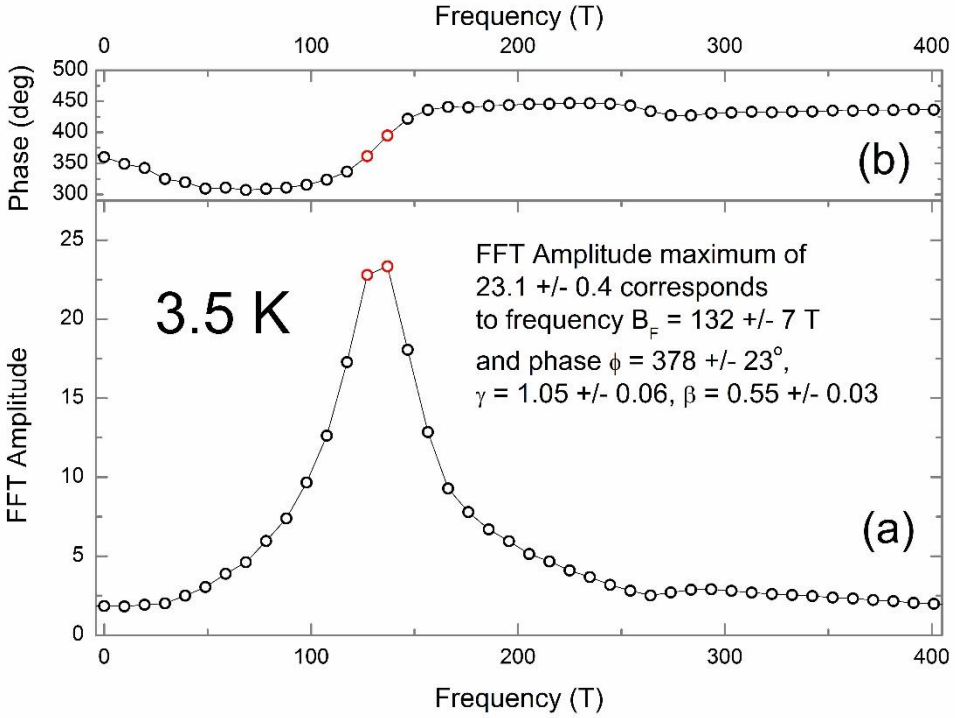

Figure 5. The FFT amplitude and phase of the SdH oscillations vs. frequency.

As evident in figure 5 (a), the contribution of harmonics higher than the first to the SdH oscillations is ~10 % or smaller, permitting utilization of the expression including only the first harmonic. Then, for the oscillating part of the resistivity one has

$$\Delta \rho_{osc} (B, T) \approx A_1 (B, T) \cos [2\pi (B_F / B - \gamma)], \quad (1)$$

where the amplitude A_1 can be expressed as

$$A_1 (B, T) = C \{x (B, T) / \sinh [x (B, T)]\} \exp [- x (B, T_D) / 2]. \quad (2)$$

Here, C is a constant, $x (B, T) = 2\pi^2 k_B T / (\hbar \omega_c)$, where k_B is the Boltzmann constant and $\omega_c = eB/m_c$ is the cyclotron frequency, m_c is the cyclotron mass (in what follows, m_c is always expressed in units of the free electron mass, m_0), and T_D is the Dingle temperature, addressed to a non-thermal expansion of the Landau levels [19-23]. For a case, when the latter is related entirely to the short-range electron scattering, T_D is connected to the transport relaxation time, τ, with the expression $T_D = T_{D\mu} \equiv \hbar / (\pi k_B \tau)$. Otherwise, deviations of T_D from $T_{D\mu}$ can be caused by inhomogeneous distribution of the electrons over a sample, leading to different B_F values in different sample points [23], and/or to a long-range nature of the scattering potential addressed e. g. to ionized impurities [24].

As follows from equation (1), the values of B_F and γ or $\beta = \gamma - 1/2$ can be obtained with the analysis of the "fan diagrams", plotting the numbers of the SdH maxima and minima, N_m, vs. reciprocal field $1/B_m$ corresponding to them. Such plots are expected to be linear, and the values of B_F and β can be obtained as the slope and the intercept with the N_m axis, respectively. The linearity of the plot of N_m vs. $1/B_m$ is evident in figure 4 (b), yielding the values of $B_F = 131.2 \pm 0.5$ T and $\beta = 0.27 \pm 0.03$, same at 3.5 and 4.2 K. One can see, however, that although B_F coincides with the value found with the FFT analysis, β is only half of the value obtained in FFT. A similar situation has been observed earlier in some investigations of the SdH effect in graphene [9, 15, 25]. At this point, probably the most comprehensive analysis performed in Ref. 25 including 12 fan diagrams, obtained at a different gate voltage, revealed that only few of them have yielded a satisfactory agreement with $\beta = 1/2$ within the error. This suggests that the fan diagrams are quite available for determination of

the SdH frequency, but may not be always a best method to find the SdH phase. The point is that the SdH phase is highly sensitive to the quality of the plots, requiring usually much more rigid conditions to the accuracy of the data points, than B_F. In this sense, the error of β on the order of ~ 10 % following from figure 4 (b), looks quite underestimated. Indeed, if we e.g. perform the fit of the plot in this figure with a second-order polynomial function, we obtain practically the same linearity and quite close value of B_F, whereas the phase value would be β = 0.12 ± 0.12. Hence, determination of β with the fan plots should be performed with a certain cautions.

The quite weak temperature dependence of $\Delta\rho_{osc}$, evident in figure 4 (a), does not permit determination of the cyclotron mass with the conventional method by analyzing the plots of A_1 (B, T) vs. T. However, this can be done by fitting the field dependence of the relative SdH amplitudes, A_1 (B, T) / A_1 (B^*, T), presented in figure 6 (a, b), where the field B^* has been taken close to the center of the investigated field interval (namely, B^* = 19.48 and 19.51 T at T = 3.5 and 4.2 K, respectively).

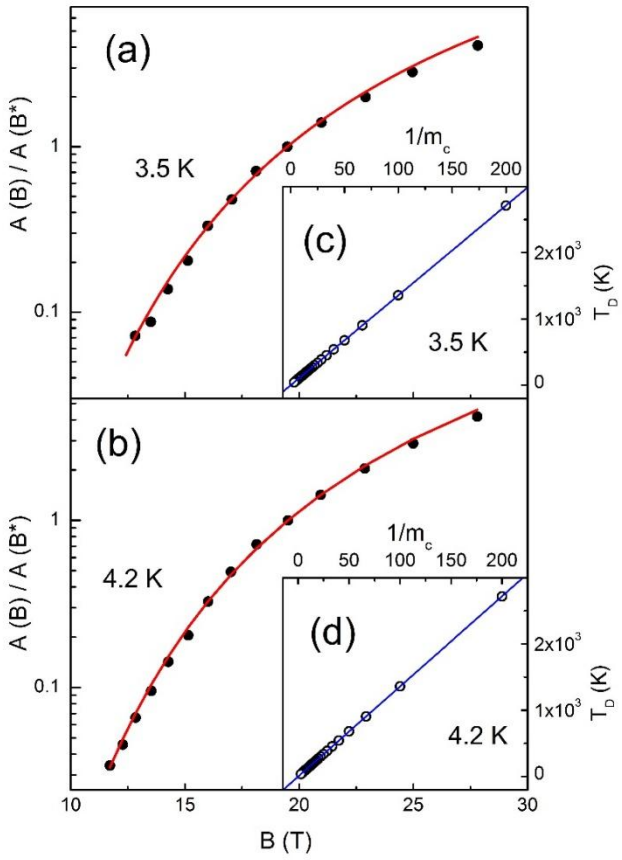

Figure 6. The dependence of the relative SdH amplitude on B at 3.5 K (a) and 4.2 K (b). The lines are calculated as described in text. The constraint function of T_D vs. $1/m_c$ at 3.5 K (c) and 4.2 K (d). The lines are linear fits.

Utilization of the amplitude ratios permits exclusion of the unknown coefficient C in equation (2), leaving only two fitting parameters, m_C and T_D. However, an attempt of a direct two-parametrical least-square fit of $A_1(B, T) / A_1(B^*, T)$ with equation (2) always leads to a mutual dependence of these parameters, yielding no certain results until one of them is known. On the other hand, although such dependence has no a physical sense, it can be used as a constraint function, limiting the possible pairs of (T_D, m_c), compatible with equation (2) and experimental $A_1(B, T)$ data. This function can be obtained in a most accurate way with the Dingle plots, following from equation (2) and the expressions of $x(B, T) = \alpha m_c T / B$, where $\alpha = 14.68$, if T is in Kelvins and B is in Teslas,

$$DP \equiv \ln \{A_1(B, T) [\sinh(\alpha m_c T / B)/(\alpha m_c T / B)]\} = \ln C - (\alpha m_c T_D /2)\times 1/B. \quad (3)$$

It can be shown that the Dingle plots, DP vs. $1/B$, are linear within a broad interval of m_c values. Therefore, the constraint function above can be obtained by variation of m_c within this interval, until the linearity of the Dingle plots is sufficiently high, and by determination of T_D (m_C) at each value of m_c from the slope of the plots. The obtained data are displayed in figure 6 (c, d) and exhibit a linear correlation between T_D and $1/m_c$, $T_D = \eta_0 + \eta_1/m_c$, where $\eta_0 = -0.78 \pm 0.08$ and -1.0 ± 0.2, as well as $\eta_1 = 13.566 \pm 0.002$ and 13.606 ± 0.005 (all in K), found with the linear fits at 3.5 and 4.2 K, respectively. Hence, finally the relative amplitudes in figure 6 (a, b) can be fitted with equation (2), using a single unknown parameter, m_c. This fit leads to the same value of $m_c = 0.07 \pm 0.01$ for both 3.5 and 4.2 K. However, one should keep in mind a similar problem in determination of the parameter η_0, as we have met above with respect to determination of β from the fan plot in figure 4 (b). Namely, it deals with the accuracy of η_0, because its error is entirely responsible for the obtained error of m_c. To minimize this error, we used up to $n_p = 30$ points of m_c taken within the interval of $\Delta m_c = 0.005 – 0.3$. So, one can see that the number of the data points and the widths of the interval of m_c in figures 7 (c, d) is ~ 2 and 6 times higher, respectively, than for the corresponding data in figure 4 (b). In addition, the accuracy of the fit in figures 6 (c, d) can be controlled by variation of n_p and Δm_c, respectively. We have found that n_p ~ 30 points is probably the optimum value, because further increase of n_p does not improve the accuracy of η_0. On the other hand, the expansion of Δm_c above 0.3 worsens the linearity of the Dingle plots substantially, which leads to a direct increase of the error of η_0.

The obtained value of $m_c = 0.07 \pm 0.01$ coincides within the error with the expected value for graphene, evaluated with the expression $m_c^* = \hbar (\pi n_e)^{1/2}/v_F$, where n_e is the electron concentration and

$v_F \approx 1.1\times10^6$ m/s is the Fermi velocity [2], yielding $m_c^* = 0.067$ (small difference between n_R and n_{SdH} is unimportant here). In addition, m_c is also close to $m_c^T \approx 0.08$, obtained recently in a similar material of graphene on SiC (0001) (exhibiting $n_e \sim (1.2 – 1.3)\times10^{13}$ cm^{-2} and $\mu_R \sim 300 – 400$ cm^2/(Vs) close to our data), with the temperature dependence of the SdH amplitude between $T \sim 4.2 – 100$ K [9]. Here, it is worth mentioning that the function x/sinh (x) which determines the temperature behavior of the SdH amplitude in equation (2), exhibits a weak dependence on x at small argument values. So, in our case we have x between ~ 0.4 – 0.1 at $B = 10 – 30$ T. Then, the variation of x/sinh (x) at 3.5 – 4.2 K is very small, lying only between 0.9 – 0.1 % at $B = 10 – 30$ T. The smallness of x, in turn, is provided by the relatively small $m_c \approx 0.07$, typical of graphene. Therefore, the weak temperature dependence of the SdH oscillation amplitude observed in Fig. 4 (a) is consistent with the small cyclotron mass.

The Dingle temperature can be obtained either with the constraint dependence above or with the slope of the Dingle plot, shown in figure 5 (c), yielding at $m_c = 0.07 \pm 0.01$ the same value of $T_D = 190 \pm 30$ K for the 3.5 and 4.2 K data. The value of $T_{D\mu} = \hbar e / (\pi\mu_R k_B m_c) \approx 200$ K coincides with T_D within the error. Hence, the non-thermal broadening of the Landau levels is connected mainly to the short-range electron scattering, supporting the sufficiently high homogeneity of distribution of the electron concentration in our material and yielding the transport time $\tau \approx 1.2\times10^{-14}$ s. It should be noted, that in graphene on SiO_2 and SiO_2/Si substrates the ratio of $T_D/T_{D\mu}$ (or, equivalently, of the transport and the quantum time, respectively), has been observed within the interval of ~ 1.5 – 5.1 deviating substantially from unity [8, 24]. Such deviations have been attributed to scattering from charged impurity residing within 2 nm of the graphene sheet, reflecting presumably an influence of the graphene/SiO_2 interface [24]. On the other hand, another type of substrate and/or a twice-smaller thickness of our film probably does not favor generation of such charge.

3.2. Analysis of MR in non-quantizing fields and zero-field resistivity

As will be evident below, it is more convenient to start the analysis in this section with the MR in non-quantizing magnetic fields. First of all, application of fields B as high as 10 T would lead to a considerable influence of a classical (CL) MR effect. Irrespective of its explicit nature, it is always positive satisfying the expression

$$(\Delta\rho/\rho)_{CL} \approx (\mu_F B)^2 \quad (4)$$

in a weak field limit of $(\mu_F B)^2 << 1$, and may obscure considerably the quantum contributions to MR. Here, μ_F is a constant on the order of the carrier mobility, but may differ from it substantially, depending on the sample sizes and geometry [26-29]. In addition, several other mechanisms may lead to another types of pMR in graphene, deviating from the quadratic field contribution to MR and not connected directly to the quantum effects as WL [30-32]. On the other hand, as can be seen in figure 7 (a), the quadratic pMR dependence of equation (4) dominates evidently within a quite broad interval of $B^2 \sim 10 - 100$ T^2, yielding $\mu_F = 125 \pm 5$ cm^2 /(Vs), comparable with $\mu_R \approx 300$ cm^2 /(Vs) (see above). Therefore, its attribution preferably to the classical MR effect looks convincing.

Nowadays it is widely believed, that in graphene the low-temperature nMR and anomalous (non-classical) pMR are connected to the WL, which existence in this material is provided by a strong intervalley and intravelley scatterings [2, 7]. If the spin-orbit interaction (SOI) is neglected, the corresponding contribution to MR can be written as

$$(\Delta\rho/\rho)_{WL} = - G_q \rho_0 \{F (B/B_\varphi) - F [B/(B_\varphi + 2B_i)] - 2F [B/(B_\varphi + B_s)]\}, \quad (5)$$

where $G_q = e^2 / (2\pi^2 \hbar) = 1.23\times10^{-5}\ \Omega^{-1}$ is a constant, $\rho_0 = 1/\sigma_0$ is the residual resistivity, $\sigma_0 = e^2 m_c v_F^2 \tau/(\pi\hbar^2) \approx 6.95\times10^{-4}\ \Omega^{-1}$ [2], $F(x) = \ln x + \psi(1/x + 1/2)$, ψ is the digamma function, $B_{\varphi, i, s} = \hbar / (4 De \tau_{\varphi, i, s})$, $D = v_F^2\tau/2 \approx 7.3\times10^{-3}$ m^2/s is the diffusion coefficient, and τ_φ, τ_i and τ_s are the phase relaxation time, the relaxation time due to the intervalley and the intravelley scatterings, respectively [2, 7].

In addition to the contributions above, the influence on the resistivity and MR from the electron-electron interaction (EEI) has been observed in graphene, too [33-35]. Such influence can be taken into account with the expression [34, 36]

$$\rho_{EEI}(B, T) = \rho_0 + [(\omega_c\tau)^2 - 1]\, G_0\, \rho_0^2\, A \ln (k_B T\tau / \hbar), \quad (6)$$

suggesting a multiple carrier scattering in the diffusive regime of $k_B T \tau / \hbar << 1$. For graphene grown on SiC, $A \approx 1 - 0.046\, c$ [34], where the parameter c is the number of multiplet channels taking part in EEI. Namely, c = 15, 7 and 3, if all the channels are possible (perfect graphene), some of them are suppressed by breaking of the time-reversal symmetry within a single valley at $T < T_s \equiv \hbar / (k_B \tau_s)$ and by the intervalley scattering at $T < T_i \equiv \hbar / (k_B \tau_i)$, respectively [34, 37].

In zero magnetic field, the corresponding contributions to the resistivity are as follows:

(i) in the absence of the quantum transport above,

$$\rho_{CL}(T) = \rho_0 + C_2 T^2 + C_5 T^5, \tag{7}$$

where C_2 and C_5 are the constants, and the second and third terms in equation (7) are addressed to the electron-electron and electron-phonon scatterings, respectively [38];

(ii) the WL contribution [2, 7],

$$\Delta \rho_{WL}(T) = \rho_0^2 G_q \{\ln(\tau^{-1}/\tau_\varphi^{-1}) - 2 \ln[\tau^{-1} / (\tau_\varphi^{-1} + \tau_s^{-1})] - \ln[\tau^{-1} / (\tau_\varphi^{-1} + 2\tau_i^{-1})]\}, \tag{8}$$

and (iii) the EEI contribution (taking into account quantum interference effects in the diffusive channel), which is given with Eq. (6) at $B = 0$.

Presence of SOI modifies equations (5) and (8) considerably. However, if SOI is performed preferably by the intrinsic Kane-Mele (KM) mechanism, then the SOI time, τ_{SO}, can be absorbed into a modified definition of the phase relaxation time,

$$\tau_\varphi^{-1} \rightarrow \tau_{\varphi t}^{-1} = \tau_\varphi^{-1} + \tau_{SO}^{-1}, \tag{9}$$

remaining otherwise equations (5) and (8) the same [2, 39].

The relaxation times above are not expected to depend on temperature, being determined by fundamental features of the graphene band structure [2], excluding τ_φ. The dependence of $\tau_\varphi(T)$ can be expressed as

$$1/\tau_\varphi(T) = A_1 T + A_2 T^2. \quad (10)$$

Here, the first and the second terms arise from the Nyquist scattering and the direct Coulomb interaction, respectively, and A_1 and A_2 are constants independent of T [2, 15, 40]. In particular, in graphene such combination has been found from the direct analysis of MR within a broad temperature range of ~ 1.9 – 45 K, but in small fields of $B < 0.12$ T [13].

As evident in figure 3 (b), MR can be fitted explicitly with the equation $\Delta\rho/\rho = (\Delta\rho/\rho)_{CL} + (\Delta\rho/\rho)_{WL} + (\Delta\rho/\rho)_{EEI}$ (the straight line), where the first and the second terms are given by equations (4) and (5), respectively, while $(\Delta\rho/\rho)_{EEI}$ is obtained with equation (6) at $c = 3$. This yields the values of the fitting parameters, $B_s \approx 0.103$ T, $B_i \approx 0.87$ T and $B_s \approx 2.27$ T. The WL and EEI contributions are displayed separately in figure 7 with the dashed and the dotted lines, respectively, along with their sum (solid line). The latter agrees completely with the difference of the experimental data and the classical contribution, $(\Delta\rho/\rho)_{exp} - (\Delta\rho/\rho)_{CL}$ (open circles in figure 7 (a)). It is noticeable, that the field dependence of the sum $(\Delta\rho/\rho)_{WL} + (\Delta\rho/\rho)_{EEI}$ is quite weak between B ~ 3 – 10 T. This permits a direct extraction of the classical contribution from the plot of Fig. 7 (a), as has been done above.

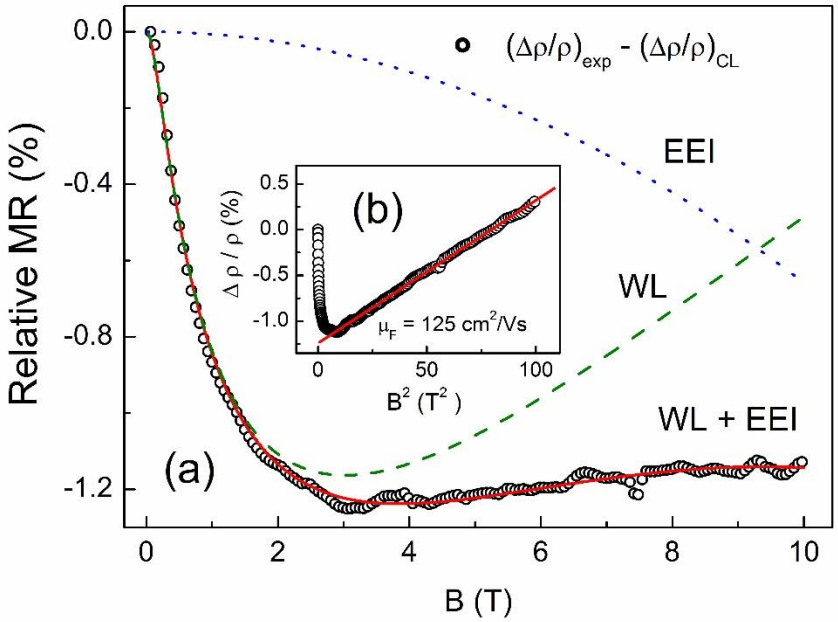

Figure 7. (a) The dependences of $(\Delta\rho/\rho)_{exp} - (\Delta\rho/\rho)_{CL}$ (circles), $(\Delta\rho/\rho)_{WL}$ (dashed line WL), $(\Delta\rho/\rho)_{EEI}$ (dotted line EEI) and $(\Delta\rho/\rho)_{WL} + (\Delta\rho/\rho)_{EEI}$ (solid line WL + EEI) on B; (b) The plot of $\Delta\rho/\rho$ on B^2. The line is linear fit.

The values of the relaxation times have been obtained with the data of B_φ, B_i and B_s, yielding $\tau_\varphi \approx 2.18\times10^{-13}$ s, $\tau_i \approx 2.58\times10^{-13}$ s and $\tau_s \approx 9.9\times10^{-15}$ s. On one hand, the choice of $c = 3$ above is supported by the value of $T_i = \hbar / (k_B\tau_i) \approx 30$ K, exceeding substantially 4.2 K – see remarks to equation (6). On the other hand, the data of the relaxation times give evidence for an inequality $\tau_\varphi < \tau_i$. However, if SOI is neglected, the negative contribution of WL to MR at $\tau_\varphi < \tau_i$ has been predicted to vanish completely [7], contradicting to the present observed picture. Therefore, such contradiction can be removed by assuming importance of SOI in our material, presented presumably by the Kane-Mele mechanism. In particular, this means, that the analysis of MR above has yielded the value of $\tau_{\varphi t}$ instead of τ_φ, which exceeds $\tau_{\varphi t}$ (see above).

Hence, the temperature dependence of the resistivity in figure 3 (a) should be analyzed with equation (6) at $B = 0$ and equation (8) with $\tau_{\varphi t}$ instead of τ_φ. In turn, instead of equation (10) we should use the expression $1/\tau_{\varphi t}(T) = A_1T + A_2T^2 + \tau_{SO}^{-1}$. Because τ_{SO} is expected to be independent of T, this time can be expressed via the quantity $\tau_{\varphi t}(4.2\text{ K}) = 1.8\times10^{-13}$ s, obtained above from the analysis of MR: $\tau_{SO}^{-1} = 1/\tau_{\varphi t}(4.2\text{ K}) - A_1\times(4.2\text{ K}) - A_2\times(4.2\text{ K})^2$. Finally, this leads to the expression

$$1/\tau_{\varphi t}(T) = A_1\times(T - 4.2\text{ K}) + A_2\times[T^2 - (4.2\text{ K})^2] + 1/\tau_{\varphi t}(4.2\text{ K}). \qquad (10')$$

The experimental dependence of $\Delta\rho(T)$ in figure 3 (a) has been fitted explicitly with the expression $\Delta\rho_{cal}(T) = \Delta\rho_{WL}(T) + \Delta\rho_{EEI}(T) + \Delta\rho_{CL}(T)$. Here, $\Delta\rho_{WL}(T)$ is calculated with equation (8) with τ_φ substituted for $\tau_{\varphi t}$, where the latter satisfies equation (10′), while the values of τ_i and τ_s are taken the same as those obtained in the MR analysis above. The function $\Delta\rho_{EEI}(T)$ is obtained with equation (6) at $B = 0$, $c = 3$ and 7 at $T < T_i$ and $T > T_i$, respectively (T_i is marked in Fig. 3 (a) with the vertical arrow), because $T_s \approx 770$ K exceeds considerably the investigated temperature range (see text below equation (6)). Finally, $\Delta\rho_{CL}(T)$ is calculated with equation (7). The fitting procedure has been performed within both temperature intervals above simultaneously. Therefore, the fitting parameters, $A_1 \approx 1.1\times10^{11}$ K^{-1}s^{-1}, $A_2 \approx 1.0\times10^{10}$ K^{-2} s^{-1}, $C_2 \approx 6.2\times10^{-3}$ Ω K^{-2} and $C_5 \approx 3\times10^{-10}$ Ω K^{-5}, are the same at all T. They yield the data of $\tau_{SO} \approx 2.5\times10^{-13}$ s and $\tau_\varphi(4.2\text{ K}) \approx 1.6\times10^{-12}$ s, where the latter exceeds substantially the value of $\tau_i \approx 2.58\times10^{-13}$ s.

4. Discussion

The analysis of the SdH effect in *Section 3.1* give a strong support, that our material represents mainly the single graphene layer with homogeneous electron distribution. Indeed, the values of β and m_c are in reasonable agreement with their predictions for graphene, while the Dingle temperature T_D is close to $T_{D\mu}$ typical of the short-range electron scattering (see Section 3.1). MR has been investigated also within the whole (and rather broad) interval of non-quantizing magnetic fields of B up to ~ 10 T, exhibiting an explicit agreement with the WL and the EEI calculations. Concerning the latter, the condition for a purely diffusive regime of equation (6), $k_B T\tau/\hbar << 1$, is well satisfied for MR at 4.2 K and for ρ (T) at all temperatures between ~ 4 – 85 K, yielding $k_B T\tau / \hbar \sim 0.01 - 0.1$. This supports the use of the equation (6) for the analysis of our MR and ρ (T) data without any limitations. At the same time, as can be obtained with equation (10) and the data of A_1, A_2 and τ found in *Section 3.2*, the values of τ_φ and τ coincide only at $T \approx 86$ K. Therefore, the WL observation condition of τ_φ (T) >> τ persists within the majority part of the investigated temperature interval, supporting applicability of the whole performed analysis of MR and ρ (T). At the same time, introduction of τ_{SO} into the analysis is important, permitting determination of a more realistic value of τ_φ. Moreover, the agreement of $\Delta\rho_{cal}$ (T) with the experimental data in figure 3 (a) is worsening considerably and takes place only asymptotically i. e. within rather narrow intervals of the highest and lowest T, if SOI is neglected. It is worth mentioning, that both the MR and ρ (T) data can be reproduced, although somewhat less accurately, even by neglecting EEI and SOI contributions at all. However, the values of τ_φ (4.2 K) = 2.5×10^{-13} s and 1.5×10^{-12} s, following from the MR and ρ (T) analyses, respectively, are in a drastic disagreement for such a case. Eventually, incorporation of SOI into the analysis of ρ (T) but neglect of EEI leads to a sharp disagreement with the experimental data.

It should be noted, that MR in figure 3 (b) can be reproduced by a single curve, whereas this is impossible for ρ (T) in figure 3 (a) due to existence of a temperature scale $T_i \approx 30$ K (see remarks to equation (6)). However, a crossover interval between ~ 20 – 50 K around T_i looks rather broad. At the same time, SOI introduces a new temperature scale $T_{SO} \equiv \hbar / (k_B\tau_{SO}) \approx 30$ K lying close to T_i, which may affect the crossover width.

Above we have assumed that τ_i and τ_s do not depend on T. However, in Ref. 15 some temperature dependence of the characteristic lengths $L_{i,s} = (D\tau_{i,s})^{1/2}$ has been observed between T ~ 2 – 45 K. On the other hand, this dependence is quite weak, lying close to the error. One should note

also, that the results of Ref. 15 have been obtained in weak magnetic fields up to $B \sim 0.1$ T to avoid influence of other effects as classical pMR and EEI. Nevertheless, as shown in Ref. 41, one cannot neglect some influence of the classical MR even in such small fields. At the same time, no temperature dependence of τ_i and τ_s has been reported in [34] within $T \sim 2 - 150$ K.

Another important assumption made above is that we presumed a domination of the intrinsic KM mechanism of SOI, which permits utilization of equation (9). However, such mechanism may be less important than the extrinsic Bychkov-Rashba (BR) process, as has been observed in graphene on the transition metal dichalcogenide substrates [41]. On the other hand, the extrinsic BR mechanism requires an external electric field, which is perpendicular to the graphene plane [42]. Such field can originate from a gate voltage and/or existence of charged impurities in the substrate. However, no gate voltage has been applied in our investigations. At the same time, no influence from the charged impurity associated with the substrate follows from our SdH data, too. Otherwise, a substantial contribution of the long-range impurity scattering would lead the ratio of $T_D/T_{D\mu}$ to lie evidently above unity, which contradicts to our result of $T_D \approx T_{D\mu}$ given at the end of *Section 3.1*. It should be also noted, that our value of $\tau_{SO} \approx 2.5\times10^{-13}$ s looks rather high to be attributed entirely to the KM mechanism, because it is very close to that of $\sim 2\times10^{-13}$ s associated with the BR process [41]. On the other hand, both SOI mechanisms above suggest a substantial dependence of τ_{SO} on τ, namely $\tau_{SO} \sim \tau$ and τ^{-1} for the KM and BR processes, respectively [2]. However, no dependence of τ_{SO} on τ has been observed in Ref. 41 within a broad interval of $\tau \sim (1 - 12)\times10^{-13}$ s. Therefore, the issues above probably do not permit to consider a situation with the SOI in graphene to be quite satisfactory in general.

In figure 3 (d) is displayed the mobility, calculated with the expression $\mu_{cal}(T) \approx 1/[e\, n_e\, \rho_{cal}(T)]$, where $\rho_{cal}(T) = \rho_0 + \Delta\rho_{cal}(T)$ and $n_e = 1.33\times10^{12}$ cm^{-3} is taken as an average value between n_R and n_{SdH}. Reasonable agreement of $\mu_{cal}(T)$ with the experimental data in Fig. 3 (d) permits to estimate the real error of both quantities at a level of ~ 5 %, which means that the SdH and the Hall concentrations coincide within this error. At the same time, no influence of EEI on the Hall coefficient according to the expression $\Delta R_H / R_H \approx 2(\Delta\rho/\rho)_{EEI}$, predicted in [36, 43], can be observed here. Indeed, as follows from Fig. 7 (a) the value of $2(\Delta\rho/\rho)_{EEI} \sim 0.01$ % at $B = 1$ T is negligible (cf. figure 3 (c)). Therefore, the error of n_R and n_{SdH} is attributable presumably to some extrinsic reasons as e.g. presence of the double-layer inclusions or some influence of the lithography process on the graphene quality.

Finally, as observed in figure 3 (a), the contribution of the electron-electron scattering exceeds considerably the influence of the electron-phonon scattering mechanism, as can be expected for a dense electronic system at low temperatures.

5. Conclusions

We have investigated quantum contributions to the magnetotransport of graphene grown on SiC (0001), within the low-temperature interval of $T \sim 4 - 85$ K in strong pulsed magnetic fields of B up to 30 T. The material characterization, performed with the Raman spectroscopy and Kelvin-probe microscopy methods, evidences for a single layer graphene with a small amount of a submicron scale double-layer inclusions. These results have been supported completely with investigations of the SdH effect observed between ~10 – 30 T, yielding the data of m_c and β quite close to the values expected for a single-layered graphene. In addition, the Dingle plot analysis gives evidence for a homogeneous distribution of the electrons over the sample, experiencing only the short-range scattering. A detailed analysis of the zero-field resistivity and magnetoresistance in non-quantizing fields permitted to establish contributions to MR from the classical effect and the quantum effects of the weak localization and the electron-electron interaction mechanisms. High importance of the spin-orbit interaction contribution has been demonstrated, too.

Acknowledgments

The authors are grateful to V Yu Davydov and P A Dementev for useful discussions of the Raman measurements and AFM data.

References

1. Graphene Nanoelectronics, ed. by Hassan Raza (Springer-Verlag, Berlin, 2012).

2. Physics of Graphene, ed. by Hideo Aoki (Springer-Verlag, Berlin, 2014).

3. F. V. Tikhonenko, A. A. Kozikov, A. K. Savchenko, and R. V. Gorbachev. 2009 Phys. Rev. Lett. 103, 226801 (2009).

4. J. Winterlin and M. L. Bocquet, Surf. Sci. 603, 1841 (2009).

5. E. Tiras, S. Ardali, T. Tiras, E. Arslan, S. Cakmakyapan, O. Kazar, J. Hassan, E. Janzben, and E. Ozbay, J. Appl. Phys.113, 043708 (2013).

6. X. Wu, X. Li, Z. Song, C. Berger and W. A. de Heer, Phys. Rev. Lett. 98, 136801 (2007).

7. E. McCann, K. Kechedzhi, V. I. Fal'ko, H. Suzuura, T. Ando, and B. L. Altshuler, Phys. Rev. Lett. 97, 146805 (2006).

8. E. Arslan, S. Ardali, E. Tiras, S. Cakmakyapan, and E. Ozbay, Phil. Mag. 97, 187 (2017).

9. N. V. Agrinskaya, A. A. Lebedev, S. P. Lebedev, M. A. Shakhov, and E. Lähderanta, Mater. Res. Express 6, 035603 (2019).

10. R. Beams, L. G. Cançado and L. Novotny, J. Phys.: Condens. Matter 27, 083002 (2015).

11. A. C. Ferrari, J. C. Meyer, V. Scardaci, C. Casiraghi, M. Lazzeri, F. Mauri, S. Piscanes, D. Jiang, K. S. Novoselov, S. Roth, and A. K. Geim, Phys. Rev. Lett. 97, 187401 (2006).

12. V. Panchal, R. Pearce, R. Yakimova, A. Tzalenchuk, and O. Kazakova, Sci. Rep. 3, 2597 (2013).

13. S. Novikov, J. Hämäläinen, J. Walden, I. Iisakka, N. Lebedeva, and A.Satrapinski, in: *16th International Congress of Metrology*, p. 13003 (2013).

14. E. Lähderanta, M. Guc, M. A. Shakhov, E. Arushanov, and K. G. Lisunov, J. Appl. Phys. 120, 035704 (2016).

15. X. C. Yang, H. M. Wang, T. R. Wu, F. Q. Huang, J. Chen, X. X. Kang, Z. Jin, X. M. Xie, and M. H. Jiang, Appl. Phys. Lett. 102, 233503 (2013)

16. Zhenbing Tan, Changling Tan, Li Ma, G. T. Liu, L. Lu, and C. L. Yang, Phys. Rev. B 84, 115429 (2011).

17. R. Akiyama, Y. Takano, E. Yukihiro, S. Ichinokura, R. Nakanishi, K. Nomura, and S. Hasegawa, Appl. Phys. Lett. 110, 233106 (2017)

18. B. Jouault, B. Jabakhanji, N. Camara, W. Desrat, A. Tiberj, J.-R. Huntzinger, C. Consejo, A. Caboni, P. Godignon, Y. Kopelevich, and J. Camassel, Phys. Rev. B 82, 085438 (2010).

19. P. T. Coleridge, R. Stoner, and R. Fletcher, Phys. Rev. B 39, 1120 (1989).

20. V. P. Gusynin and S. G. Sharapov, Phys. Rev. B **71**, 125124 (2005).

21. S. G. Sharapov, V. P. Gusynin, and H. Beck, Phys. Rev. B 69, 075104 (2004).

22. A. Isihara and L. Smrcka, J. Phys. C 19, 6777 (1986).

23. I. M. Tsidil'kovskii, Electrons and Holes in Semiconductors (Moscow, Nauka, 1972).

24. X. Hong, K. Zou and J. Zhu, Phys. Rev. B 80, 241415(R) (2009).

25. Y. Zhang, Y.-W. Tan, H.L. Stormer, P. Kim, Nature 438, 201 (2005).

26. Kireev, P. S. Semiconductor physics, p. 696 (Moscow, Mir Publishers, 1978)

27. Askerov, B. M. Electron Transport Phenomena in Semiconductors, p. 416 (Singapore, World Scientific, 1994).

28. Hari Singh Nalwa. Handbook of thin film materials: Nanomaterials and magnetic thin films. Academic Press, vol. 5, p. 514 (2002).

29. Vorob'ev V. N. and Sokolov Yu. F., Sov. Phys. Semicond. 5, 616 (1971).

30. Peng Li, Qiang Zhang, Xin He, Wencai Ren, Hui-Ming Cheng, and Xi-xiang Zhang, Phys. Rev. B 94, 045402 (2016)

31. Simon Branchaud, Alicia Kam, Piotr Zawadzki, François M. Peeters, and Andrew S. Sachrajda, Phys. Rev. B 81, 121406R (2010).

32. Zakaria Moktadir and Hiroshi Mizuta, J. Appl. Phys. 113, 083907 (2013).

33. B. Jouault, B. Jabakhanji, N. Camara, W. Desrat , C. Consejo, and J. Camasse, Phys. Rev. B 83, 195417 (2011).

34. J. Jobst, D. Waldmann, I. V. Gornyi, A. D. Mirlin, and H. B. Weber, Phys. Rev. Lett. 108, 106601 (2012).

35. B. Jabakhanji, D. Kazazis, W. Desrat, A. Michon, M. Portail, and B. Jouault, Phys. Rev. B, 035423 (2014).

36. A. Houghton, J. R. Senna, and S. C. Ying, Phys. Rev. B, 2196 (1982).

37. A. A. Kozikov, A. K. Savchenko, B. N. Narozhny, and A. V. Shytov, Phys. Rev. B 82, 075424 (2010).

38. A. A. Abrikosov, Fundamentals of the Theory of Metals (North-Holland, Amsterdam, 1988).

39. E. McCann and V I. Fal'ko, Phys. Rev. Lett. 108, 166606 (2012).

40. D. K. Ki, D. Jeong, J. H. Choi, H. J. Lee, and K. S. Park, Phys. Rev. B 78, 125409 (2008).

41. Zhe Wang, Dong-Keun Ki, Jun Yong Khoo, Diego Mauro, Helmuth Berger, Leonid S. Levitov, and Alberto F. Morpurgo, Phys. Rev X 6, 041020 (2016).

42. S. Konschuh, M. Gmitra, and J. Fabian, Phys. Rev. B 82, 245412 (2010).

43. B. L. Altshuler and A. G. Aronov, Electron-electron interaction in disordered conductors, in: Electron-electron interactions in disordered systems (Elsevier, Amsterdam, 1985).